A Basic Study of the VTOL Ground Effect Problem for Planar Flow

D. R. Kotansky* and W. W. Bower†
McDonnell Douglas Corporation, St. Louis, Mo.

The force interaction between airframe undersurfaces and the ground in the presence of lift jets is an important consideration for VTOL aircraft design. As a first step toward prediction of this phenomenon, a combined theoretical and experimental investigation of planar turbulent jet impingement flowfields has been undertaken. Unvectored jets in close ground effect have been modeled using the incompressible Reynolds equations with a one-equation turbulence model. Distributions of the flow properties are computed as functions of undersurface shape, length scales, and jet exit height above ground. Computed flowfield properties are presented and comparisons are made with experimental measurements.

Nomenclature

C_D = empirical constant in turbulence model
c_μ = empirical constant in turbulence model
$\bar{D}$ = jet slot width at exit plane (used as normalizing parameter for all lengths)
F = conformal mapping function
H = height of jet exit plane above ground normalized by $\bar{D}$
i = $\sqrt{-1}$
k = turbulent kinetic energy normalized by $\bar{V}_0{}^2$
l_D = length scale for dissipation normalized by $\bar{D}$
l_μ = length scale for viscosity normalized by $\bar{D}$
p = static pressure normalized by $\bar{\rho}\bar{V}_0{}^2/2$
Q = mapping modulus
Re = Reynolds number based on properties at jet exit plane, $\bar{V}_0\bar{D}/\bar{\nu}$
u = velocity component in x direction normalized by $\bar{V}_0$
$\bar{V}_j$ = jet velocity
$\bar{V}_0$ = jet centerline velocity at exit plane
v = velocity component in y direction normalized by $\bar{V}_0$
W = width of solution domain normalized by $\bar{D}$
w = velocity component in z direction normalized by $\bar{V}_0$
x = Cartesian coordinate normalized by $\bar{D}$
y = Cartesian coordinate normalized by $\bar{D}$
α = coefficient in general form of transport equation
β = coefficient in general form of transport equation
$\Gamma_{k,\mathrm{eff}}$ = effective transfer coefficient for diffusion normalized by $\bar{\rho}\bar{V}_0\bar{D}$
γ = coefficient in general form of transport equation
η = mapping coordinate normalized by $\bar{D}$
δ = coefficient in general form of transport equation
μ = molecular viscosity normalized by $\bar{\rho}\bar{V}_0\bar{D}$
μ_{eff} = effective viscosity normalized by $\bar{\rho}\bar{V}_0\bar{D}$
μ_{turb} = turbulent (eddy) viscosity normalized by $\bar{\rho}\bar{V}_0\bar{D}$
ξ = mapping coordinate normalized by $\bar{D}$
$\bar{\rho}$ = mass density
σ = source term in general form of transport equation
$\sigma_{k,\mathrm{turb}}$ = turbulent Prandtl number
ϕ = general flow variable
ψ = stream function normalized by $\bar{V}_0\bar{D}$
ω = vorticity normalized by $\bar{V}_0/\bar{D}$
$\overline{(\quad)}$ = (overbar) dimensional quantity
$\langle\ \rangle$ = time-averaged quantity
$(\ )'$ = fluctuating component
∞ = ambient conditions

Introduction

Background

OVER the last ten years, the interest in jet and fan-powered vertical takeoff and landing (VTOL) military aircraft has increased. During this time, numerous analytical and experimental studies of propulsion-induced aerodynamic effects have been performed in an effort to provide performance prediction methods for a range of aircraft configurations and operating conditions.

These studies have largely concentrated on the hover mode of VTOL flight, in which the suck-down, fountain formation, and hot-gas ingestion resulting from the induced flows and the interaction of the lift jets and the ground are not fully understood. These lift-system-induced aerodynamic effects cannot be easily predicted either theoretically or from scaled experiments. The numerous variables which affect the flowfield make it costly to study an aircraft configuration through wind-tunnel tests. Moreover, the three-dimensional (3-D) flow is so complicated that a rigorous analytical treatment is not possible at this time.

In order to gain a fundamental understanding of a less complex lift-jet-induced flow, the McDonnell Douglas Research Laboratories (MDRL) has conducted an investigation of the flowfield created by a single 2-D (planar) lift jet in ground effect. The primary phenomenon under study is suck-down, which results when turbulent jet entrainment induces a flow about the aircraft that leads to below-ambient static pressures on the surfaces adjacent to the jet exit. For the planar configuration, experimental data can be more easily acquired and correlated, and solutions of the governing 2-D conservation equations are readily obtained. Information from a study of this simplified configuration can then be used to understand the more complex 3-D lift-jet flowfields associated with VTOL aircraft, in particular the turbulent entrainment phenomena, just as the results of 2-D airfoil and internal flow studies have been used in practical aerodynamic and propulsion research.

To achieve this objective, MDRL has undertaken a combined experimental and theoretical research effort. The ex-

---

Presented as Paper 77-614 at the AIAA/NASA Ames V/STOL Conference, Palo Alto, Calif., June 6-8, 1977; submitted June 20, 1977; revision received Dec. 27, 1977.

Index categories: Ground Effect Machines; Subsonic Flow; Viscous Nonboundary-Layer Flows.

*Senior Scientist, McDonnell Douglas Research Lab. Member AIAA.

†Research Scientist, McDonnell Douglas Research Lab. Associate Fellow AIAA.

perimental phase of the work is the acquisition of detailed measurements for a planar lift jet issuing from a static upper surface in ground effect, and the analytical phase is a solution of the 2-D time-averaged conservation equations for the same configuration. Although test data have been reported for a single axisymmetric jet striking a ground plane,[1-4] extensive measured and calculated flow properties are not available for the planar configuration. The latter was selected for the present study for the reasons just stated and because the vectored planar jet flowfield can be computed with a 2-D analysis, while the vectored axisymmetric jet presents a fully 3-D problem.

Problem Definition

The planar unvectored impinging jet flow treated in the present paper is shown schematically in Fig. 1. The jet exits from a slot of width $\bar{D}$ in a contoured upper surface a distance $\bar{H}$ above the ground plane. The region of interest extends a distance $\bar{W}$ on each side of the jet centerline.

The jet flowfield can be divided into three regions: a free-jet region in which the flow is essentially the same as that of a jet issuing into an unbounded medium; the impingement region, where the flow changes direction with a large pressure gradient; and the wall-jet region in which the flow spreads over the ground plane surface with zero pressure gradient. The fluid surrounding the jet is entrained at the boundaries of all three regions, causing otherwise static air to be placed in motion to induce locally reduced static pressures and, thereby, an aerodynamic load on the upper surface.

In this paper, measured and computed flow properties are presented as functions of H (the jet exit height above ground normalized by the jet slot width) and Reynolds number based on conditions at the jet exit plane. Conclusions are drawn with regard to characteristics of the flowfield and the accuracy of the theoretical model, and recommendations are made for further study of the 2-D ground effect problem.

Experimental Study

Test Configuration

To experimentally investigate the viscous flowfield occurring between a simulated airframe undersurface and the ground in the presence of a planar lift jet, shown schematically in Fig. 1, the test configuration illustrated in Fig. 2a was constructed. The basic components of the arrangement are the test model, the side plates used as an aid in achieving 2-D flow, and the adjustable-height groundboard.

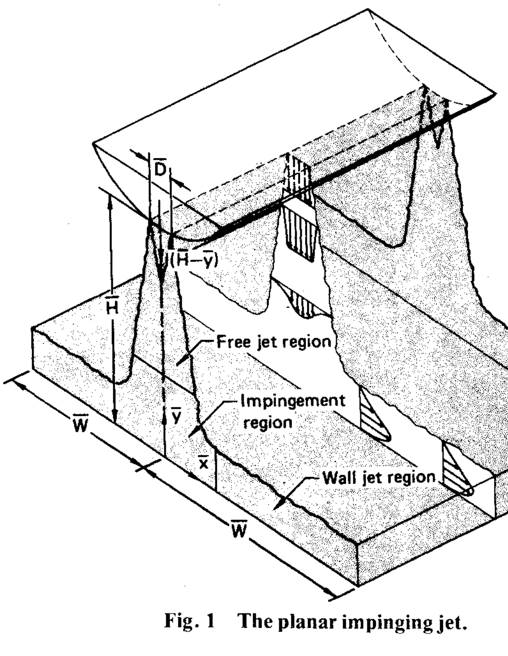

Fig. 1 The planar impinging jet.

Air is brought from two supply lines to the high-pressure plenum of the test model, shown in cross section in Fig. 2b, at a pressure in excess of 2.07×10^3 kPa (300 psi). Thus, large lateral velocities are eliminated in the air supply to the upper chamber. The first stage of pressure reduction occurs through a heavy porous plate with approximately 4% open area. Subsequent pressure reductions occur through a second porous plate and a jet exit screen with approximate porosities of 30% and 60%, respectively.

The nozzle and plenum assembly can be rotated 30 deg on either side of the model centerline to treat vectored, as well as unvectored, jet configurations. The high-pressure plenum assembly is structurally independent of the outer body to facilitate changes in body shape. In the test series conducted, measurements were made for the curved-plate model shown in Fig. 2b and also for a flat-plate model. For these configurations, extensive static pressure measurements, jet plume total pressure surveys, and hot-wire anemometer measurements were made for various values of jet height above ground and Reynolds number.

Test Results

Initially, measurements were made to establish the two-dimensionality of the planar impinging jet flow. Figure 3 illustrates, for example, measured jet dynamic pressure profiles at three stations below the jet exit on the flat-plate model. Clearly, the jet is symmetrical about the centerline. In addition, these profiles indicate a fairly well-behaved turbulent jet with a core flow persisting to approximately four diameters from the jet exit plane.

Figure 4a gives the dimensionless static pressure distributions for the undersurface of the flat-plate model and the ground surface below the flat-plate model for three values of H in close ground effect. The pressure has been normalized by $\bar{\rho}\bar{V}_0{}^2/2$, where $\bar{\rho}$ is the constant fluid density and $\bar{V}_0$ is the

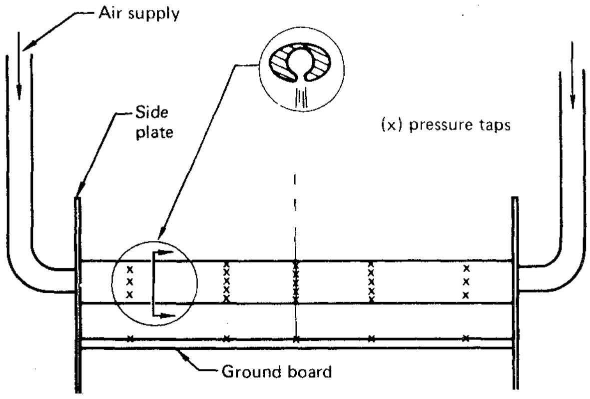

a) Test configuration and instrumentation detail

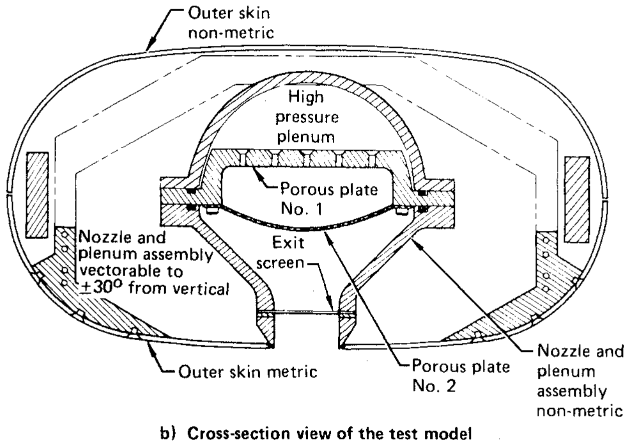

b) Cross-section view of the test model

Fig. 2 Description of the planar lift-jet/airframe/ground interaction experimental configuration.

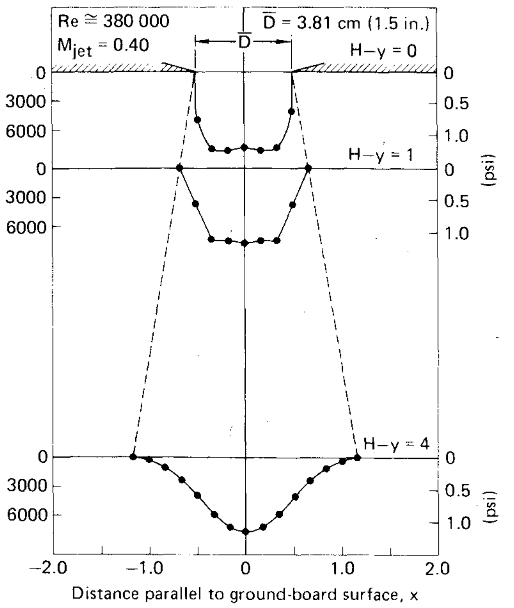

Fig. 3 Two-dimensional jet dynamic pressure profiles below flat-plate model out of ground effect.

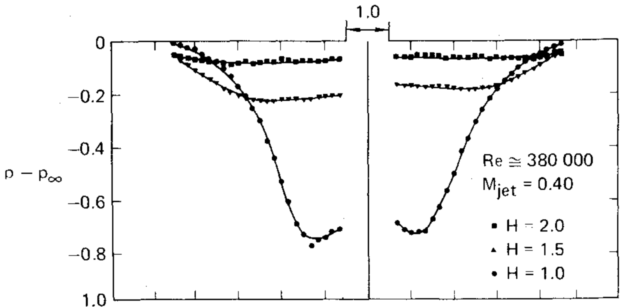

a) Under-surface static pressure profiles

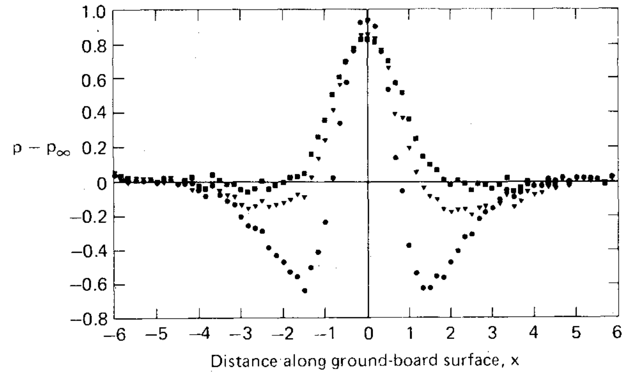

b) Ground-board static pressure profiles

Fig. 4 Measured pressure distributions for the flat-plate model in close ground effect.

jet-exit centerline velocity. The flow conditions for the data in Fig. 4 are the same as those for the free-jet profiles shown in Fig. 3. The maximum induced negative pressure measured was 6 kPa, and in all other runs induced static pressures were substantially smaller. These small pressure signals necessitated the use of a 7 kPa. (1.0 psid) transducer in the scanivalve pressure system for model surface pressures.

The pressure profiles indicate good symmetry in the flow down to $H=1$, and a strong sensitivity to H. The ground-plane static pressure distributions shown in Fig. 4b indicate some surprising results. For $H \leq 2$, ground-plane pressures on either side of the stagnation point are below ambient. These data suggest a strong acceleration in the impingement flow to either side of the stagnation point, probably a result of flow separation on the upper surface near the jet exit.

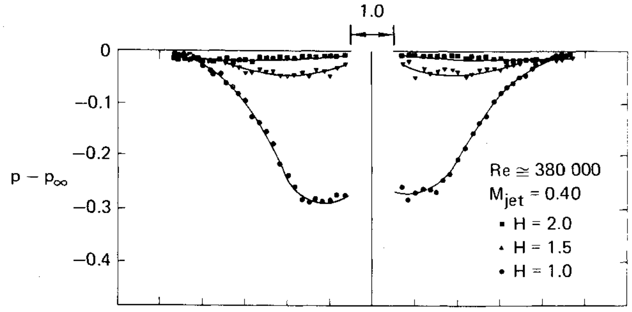

a) Under-surface static pressure profiles

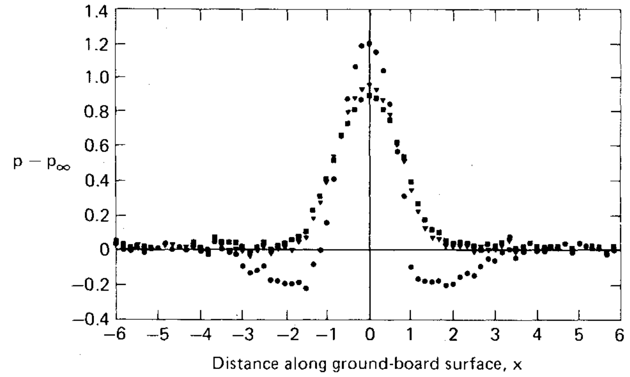

b) Ground-board static pressure profiles

Fig. 5 Measured pressure distributions for the curved-plate model in close ground effect.

Figure 5a presents the undersurface and ground-plane normalized static pressure distributions for the curved-plate model in close ground effect. The test conditions for the data shown in Fig. 5a correspond to those for the flat-plate model flowfield described previously. The sensitivity of the induced pressures on the model undersurface to H is of the same order of magnitude as for the flat-plate model. However, the magnitudes of the induced negative pressures on the curved-plate model are significantly lower (more than by a factor of two), clearly indicating the advantage of undersurface curvature in reducing induced suck-down loads for VTOL aircraft in ground effect. The below-ambient groundboard pressures are again evident in Fig. 5b for $H=1$, but they are greatly reduced from those for the flat-plate model. Comparison of Figs. 4a and 5a suggests that contouring base area away from lift nozzle exits and perhaps the use of nozzle exit extensions will significantly reduce aircraft undersurface suck-down loads.

In addition to the extensive static pressure distributions measured during the test program, complete sets of hot-wire anemometer data were taken with $H=2$ and 4 for two jet-exit Reynolds numbers in the flowfield of the oval mode. In these measurements, which were made with a two-component, hot-film anemometer system, all three components of mean and fluctuating velocities (u,v,w and u',v',w') were measured across the jet exit, along the jet centerline, and through the wall jet on the side of the flowfield from the ground plane to the shoulder height of the oval model.

Typical results of the hot-wire measurements are shown in Fig. 6 for $H=2$ and 4 with a Reynolds number of 130,000. The turbulent kinetic energy profile, normalized by $\bar{V}_0{}^2$, $k=\frac{1}{2}\langle (u')^2+(v')^2+(w')^2\rangle$, measured along the jet centerline is shown in Fig. 6a. As the curved-plate model is moved closer to the ground plane, there is an increase in the level of turbulence on the jet axis. This turbulence change is reflected in an increased decay of the jet centerline velocity, shown in Fig. 6b. It should be noted that for the case with $H=4$, the deceleration to the stagnation point becomes significant approximately two diameters below the jet exit plane; while for the case with $H=2$, the flow decelerates

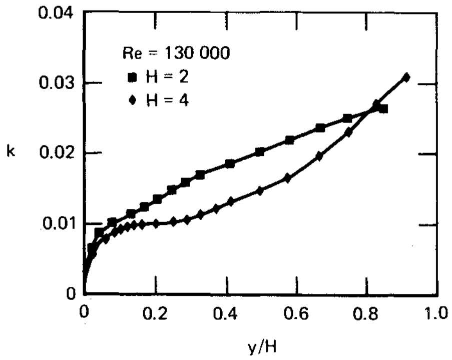

a) Jet centerline turbulent-kinetic-energy distribution

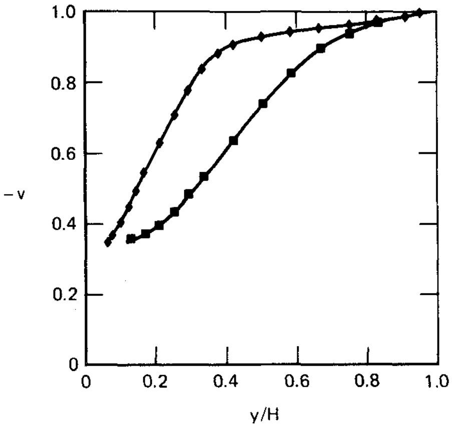

b) Jet centerline velocity distribution

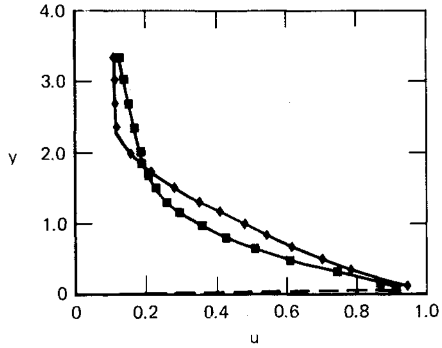

c) Wall-jet velocity profile

Fig. 6 Hot-wire anemometer measurements for the curved-plate model in close ground effect.

significantly immediately after leaving the exit slot. Figure 6c indicates conventional turbulent wall-jet profiles at the right edge of the flowfield, with increased velocities in the x direction as the height of the curved-plate above ground is reduced.

The experimental data obtained from these flowfields show the appreciable influence of the measured properties on H and the surprisingly strong effect of the body undersurface shape on the flowfield. The data also provide a means for evaluating and subsequently improving the accuracy of analytical models of the planar impinging jet flow – a topic to be considered in the following section.

Analytical Study

Governing Equations

For the flowfield configuration of Fig. 1, a rigorous fluid dynamic analysis cannot be made using purely inviscid-flow calculation techniques, even with the addition of empirical or boundary-layer corrections. With strong pressure gradients in both coordinate directions, including separation, it is clear that a turbulent boundary-layer procedure cannot be simply patched into an inviscid scheme.

In the present approach, the time-averaged continuity and Navier-Stokes equations for steady planar incompressible flow, written in terms of vorticity and stream function, are used to describe the mean motion of the fluid in the turbulent jet impingement problem. Through the averaging procedure, unknown turbulent stress terms arise which are computed using a turbulent kinetic energy equation proposed by Wolfshtein,[5] in combination with a phenomenological equation that relates the square root of the turbulent kinetic energy to the turbulent viscosity. The resulting coupled nonlinear elliptic partial-differential equations are solved for the fluid properties employing conformal mapping and finite-difference procedures.

Details of the derivation of the vorticity/stream-function form of the time-averaged conservation and turbulence model equations are presented in Ref. 6. The resulting equations are:

Poisson equation for stream function

$$\frac{\partial^2\psi}{\partial x^2}+\frac{\partial^2\psi}{\partial y^2}=-\omega \tag{1}$$

Vorticity transport equation

$$\begin{aligned}&(1+Re\mu_{\text{turb}})\frac{\partial^2\omega}{\partial x^2}-Re\left(\frac{\partial\psi}{\partial y}-2\frac{\partial\mu_{\text{turb}}}{\partial x}\right)\frac{\partial\omega}{\partial x}\\&+(1+Re\mu_{\text{turb}})\frac{\partial^2\omega}{\partial y^2}+Re\left(\frac{\partial\psi}{\partial x}+2\frac{\partial\mu_{\text{turb}}}{\partial y}\right)\frac{\partial\omega}{\partial y}\\&=Re\left[4\frac{\partial^2\psi}{\partial x\partial y}\frac{\partial^2\mu_{\text{turb}}}{\partial x\partial y}+\frac{\partial^2\psi}{\partial x^2}\left(\frac{\partial^2\mu_{\text{turb}}}{\partial x^2}-\frac{\partial^2\mu_{\text{turb}}}{\partial y^2}\right)\right.\\&\left.-\frac{\partial^2\psi}{\partial y^2}\left(\frac{\partial^2\mu_{\text{turb}}}{\partial x^2}-\frac{\partial^2\mu_{\text{turb}}}{\partial y^2}\right)\right]\end{aligned} \tag{2}$$

Turbulent-kinetic-energy equation

$$\begin{aligned}&\left(1+\frac{Re\mu_{\text{turb}}}{\sigma_{k,\text{turb}}}\right)\frac{\partial^2k}{\partial x^2}+Re\left(\frac{1}{\sigma_{k,\text{turb}}}\frac{\partial\mu_{\text{turb}}}{\partial x}-\frac{\partial\psi}{\partial y}\right)\frac{\partial k}{\partial x}\\&+\left(1+\frac{Re\mu_{\text{turb}}}{\sigma_{k,\text{turb}}}\right)\frac{\partial^2k}{\partial y^2}+Re\left(\frac{1}{\sigma_{k,\text{turb}}}\frac{\partial\mu_{\text{turb}}}{\partial y}-\frac{\partial\psi}{\partial x}\right)\frac{\partial k}{\partial y}\\&=Re\left\{\frac{C_Dk^{3/2}}{l_D}-\mu_{\text{turb}}\left[4\left(\frac{\partial^2\psi}{\partial x\partial y}\right)^2+\left(\frac{\partial^2\psi}{\partial y^2}-\frac{\partial^2\psi}{\partial x^2}\right)^2\right]\right\}\end{aligned} \tag{3}$$

Poisson equation for static pressure

$$\begin{aligned}\frac{\partial^2p}{\partial x^2}+\frac{\partial^2p}{\partial y^2}=4&\left[\frac{\partial^2\psi}{\partial x^2}\frac{\partial^2\psi}{\partial y^2}-\left(\frac{\partial^2\psi}{\partial x\partial y}\right)^2-\frac{\partial\mu_{\text{turb}}}{\partial x}\frac{\partial\omega}{\partial y}\right.\\&+\frac{\partial\mu_{\text{turb}}}{\partial y}\frac{\partial\omega}{\partial x}+\frac{\partial^2\psi}{\partial x\partial y}\left(\frac{\partial^2\mu_{\text{turb}}}{\partial x^2}-\frac{\partial^2\mu_{\text{turb}}}{\partial y^2}\right)\\&\left.-\frac{\partial^2\mu_{\text{turb}}}{\partial x\partial y}\left(\frac{\partial^2\psi}{\partial x^2}-\frac{\partial^2\psi}{\partial y^2}\right)\right]\end{aligned} \tag{4}$$

where

$$\mu_{\text{turb}}=c_\mu k^{1/2}l_\mu \tag{5}$$

$$\mu_{\text{eff}}=1/Re+\mu_{\text{turb}} \tag{6}$$

and

$$\Gamma_{k,\,\mathrm{eff}} = 1/Re + \mu_{\mathrm{turb}}/\sigma_{k,\mathrm{turb}} \tag{7}$$

The turbulence modeling constants C_D and c_μ and the length scales l_D and l_μ are specified in Ref. 6. The length scales are an important element of the turbulent-flow analysis, in that they significantly influence the level of the turbulent viscosity throughout the field. Both l_D and l_μ are dependent on the geometry of interest and are best determined on the basis of a measured turbulent kinetic energy distribution, specifically in the stagnation-point and separated regions of the flowfield. However, because detailed measurements were lacking at the time the analytical model was formulated, the length of scales presented in Ref. 6 have been established solely on the basis of simple order-of-magnitude physical arguments. As the required test data describing the local turbulent flowfield become available, l_D and l_μ can be modified to provide an accurate representation of the flow.

Equations (1-7) have been written in dimensionless form by using the normalizing parameters $\bar{D}$ (the jet width at the exit plane), $\bar{V}_0$ (the jet centerline velocity at the same station), and $\bar{\rho}$ (the constant fluid density). Dimensionless variables were obtained by dividing lengths by $\bar{D}$, the vorticity by $\bar{V}_0/\bar{D}$, the stream function by $\bar{V}_0\bar{D}$, the turbulent kinetic energy by $\bar{V}_0{}^2$, the effective and turbulent viscosities by $\bar{\rho}\bar{V}_0\bar{D}$, and the static pressure by $\bar{\rho}\bar{V}_0{}^2/2$. This normalization introduces the Reynolds number based on properties at the jet exit plane.

To solve the governing equations for a flow with a contoured upper boundary to simulate the lower surface of a fuselage, a conformal mapping procedure is introduced. In this technique, which was originally devised at MDRL by G. H. Hoffman, a finite-difference computational plane with coordinates (ξ,η) is specified. The distance between nodes in the ξ direction is a, and the distance in the η direction is b, where a and b are not necessarily equal. A conformal mapping given by

$$\xi + i\eta = F(x+iy) \tag{8}$$

is introduced which determines the physical plane (x,y). Laplace's equation is satisfied by both x and y and is solved for each variable subject to the required boundary conditions. The latter follow from physical constraints when they are known at the boundaries and from integration of the Cauchy-Riemann relations for x and y when the boundary distributions are not known. The derivatives in these equations are rewritten in terms of the computational plane coordinates and a mapping modulus Q.

Figure 7 illustrates the physical and computational planes used in the calculation of the curved-plate flowfields, along with the boundary conditions imposed on the primary flow variables (stream function, vorticity, and the turbulent kinetic energy). Since only normal impingement is considered, geometric symmetry about the jet centerline exists so that only half the flowfield need be solved. The stream function and voriticity are antisymmetric about the centerline, and the turbulent kinetic energy is symmetric. Boundary conditions imposed on ψ,ω, and k follow from the no-slip impermeable wall constraint at the solid surfaces, from symmetry at the jet centerline, and from the assumption of no gradients in the ξ direction at the right boundary. The last boundary condition is not accurate for relatively small values of W; in these cases, experimental data should be used to better define the flow properties.

With conformal mapping, the elliptic partial differential equations that describe the flow can be written in the form

$$\alpha\frac{\partial^2\phi}{\partial\xi^2} + \gamma\frac{\partial\phi}{\partial\xi} + \beta\frac{\partial^2\phi}{\partial\eta^2} + \delta\frac{\partial\phi}{\partial\eta} = \sigma \tag{9}$$

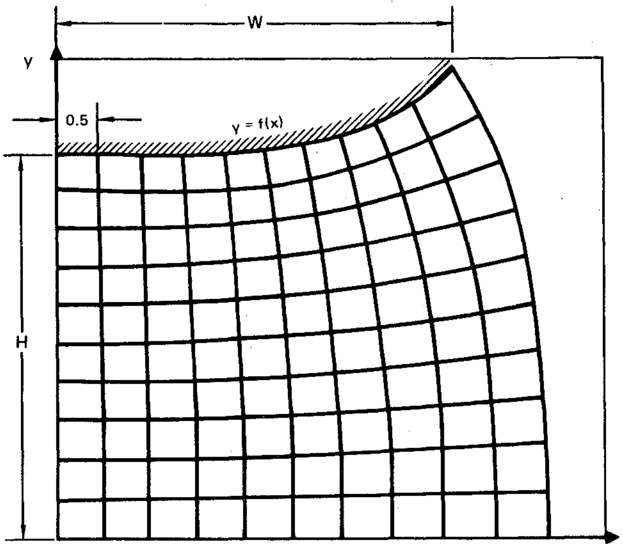

a) Physical plane

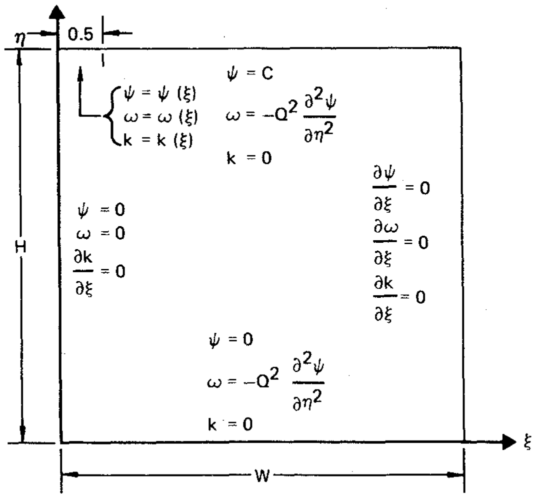

b) Computational plane

Fig. 7 Specification of the boundary conditions for the primary flow variables.

where α, γ, β, and δ denote the nonlinear coefficients, and σ denotes the source term. For the two Poisson equations, $\phi=\psi$ or $\phi=p$, Eq. (9) can be solved numerically without difficulty using the conventional central difference (CD) finite-difference algorithm. For the vorticity transport equation, $\phi=\omega$, and for the turbulence model equation, $\phi=k$, the CD algorithm cannot be used. The coefficients for these equations contain the Reynolds number as a multiplicative factor, and as a result, with the standard CD algorithm, the discretized system is diagonally dominant for only a limited range in the coefficients γ and δ. Diagonal dominance is necessary to obtain convergence in the iterative solutions of the discretized system of equations. Consequently, in the present work the voriticity transport equation and the turbulent kinetic energy equation are solved using the augmented central difference (ACD) algorithm.[6]

The finite-difference form of the flow equations is solved iteratively using point relaxation. First, a convergent solution of the Poisson equation for stream function, the vorticity transport equation, and the turbulent kinetic energy equation is obtained. Then the primitive flow variables (static pressure and the velocity components) are calculated. The Poisson equation for static pressure is solved subject to the boundary conditions on the normal pressure gradients imposed by the two time-averaged momentum equations for planar flow, and the velocity components are computed from the defining equation for the stream function. The numerical calculations were performed on the CYBER 173 system of the McDonnell Douglas Automation Company.

Analytical Results

Flowfields have been computed for the planar impinging jet illustrated in Fig. 1 with both flat- and curved-plate upper surfaces and with various values of H and Re. In this section, representative contour plots of the calculated flow variables are presented, and comparisons are made between measured and predicted flowfield properties.

For a flat upper surface, conformal mapping is not required, and the computational plane illustrated in Fig. 7 coincides with the physical plane ($\xi = n$, $\eta = y$). For this parallel-plate configuration, the flowfield model was solved with $H = 2$, $W = 4.68$, and $Re = 10{,}000$.

The primary flow variables (normalized vorticity, stream function, and turbulent kinetic energy) are shown in Fig. 8. Vorticity is convected to the right boundary of the solution domain with development of an attached boundary layer on the lower surface and a separated boundary layer on the upper surface. (Separation occurs on a solid boundary where $\omega = 0$, and in the present configuration this occurs near the slot edge.) The region of recirculating flow and the resulting entrainment into the free-jet region are clearly illustrated by the stream function plot. With regard to the turbulent kinetic energy contour, the maximum value of k imposed on the entering jet is 0.04 with a decay from this value throughout the field. Over the right half of the solution domain, the turbulent kinetic energy is fairly uniform.

The primitive flow variables (velocity components and static pressure) are given in Fig. 9. The contour plots of the two velocity components define in detail the region of recirculation between the plates. The distribution of the x component of velocity illustrates the upper- and lower-wall boundary layers and the entrainment of fluid into the jet. The sharp pressure gradient in the impingement region is shown in the plot of static pressure, where the value of p at the stagnation point has been set equal to one.

For the curved-plate upper surface, solutions have been obtained for $H = 2$ and 4 with $Re = 1000$, 10,000, and 100,000. The effect of reducing H from 4 to 2 while maintaining the Reynolds number constant is to accelerate the flow toward the right boundary of the solution domain. The dominant effect of increasing Re with fixed H is to raise the level of turbulence generation near the stagnation point.

Figures 10 and 11 contain the contour plots of the primary and primitive flow variables for the curved-plate geometry with $H = 2$, $W = 3.68$, and $Re = 100{,}000$. For this configuration, the basic flow characteristics observed in the solutions of the flat-plate geometry are again apparent: a strong convection of vorticity toward the right boundary with separation near the slot edge, a region of recirculating flow with fluid entrained into the free-jet, and strong pressure gradients in going toward the stagnation point along the jet centerline and the lower wall. One significant difference noted between the flat- and curved-plate solutions is that the upper surface pressure level is more nearly ambient for the contoured upper surface. This result is expected and has been observed in the experimental data.

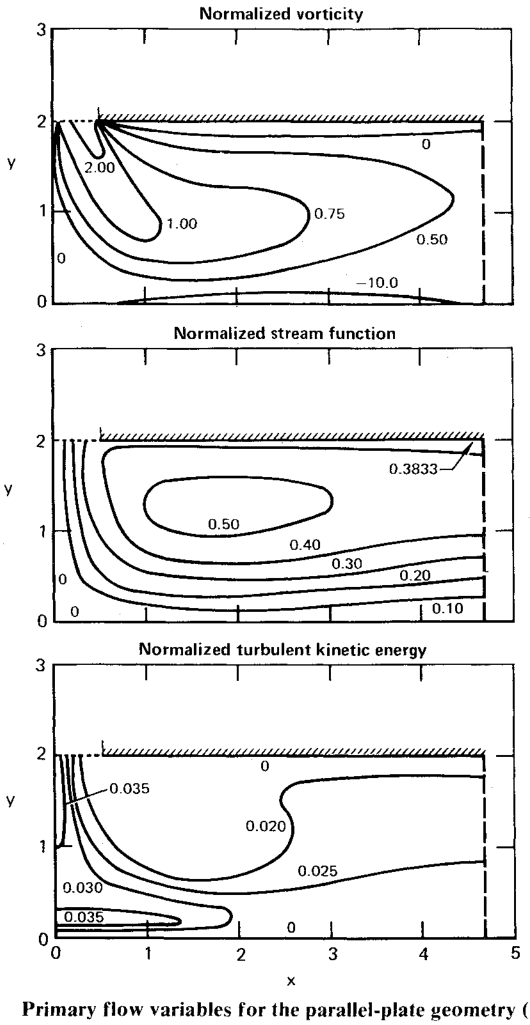

Fig. 8 Primary flow variables for the parallel-plate geometry ($H = 2$, $W = 4.68$, $Re = 10{,}000$).

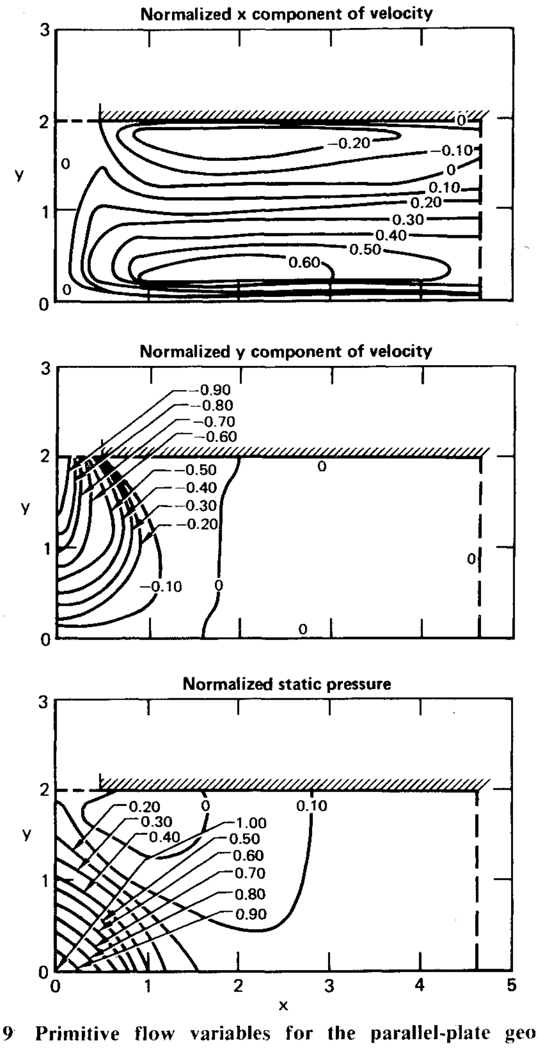

Fig. 9 Primitive flow variables for the parallel-plate geometry ($H = 2$, $W = 4.68$, $Re = 10{,}000$).

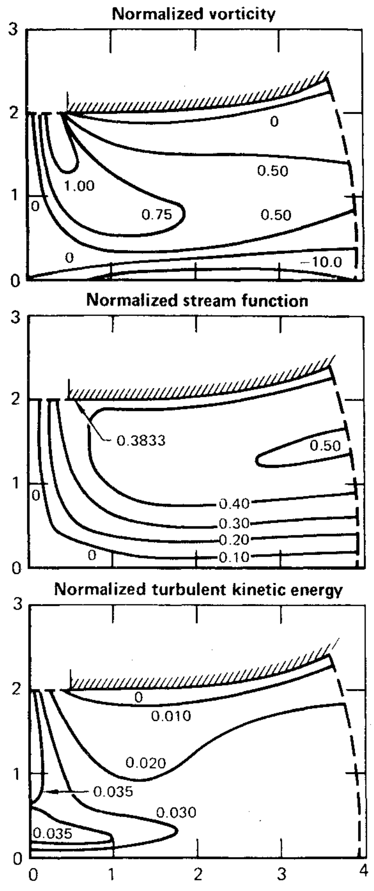

Fig. 10 Primary flow variables for the curved-plate geometry ($H=2$, $W=3.68$, $Re=100{,}000$).

Specific comparisons between measured and computed data for the curved-plate geometry with $H=2$ are shown in Fig. 12. In the analytical pressure distribution, Fig. 12a, the pressure values at the end-points of the right boundary have been used for p_∞ at each surface to compare with the data. The computed normalized profiles of $p-p_\infty$ reproduce the large lower-wall pressure drop in the impingement region and the relatively constant low-pressure level along the upper surface. Good agreement between the measured and computed centerline velocity variations was also obtained (Fig. 12b).

Comparisons of theoretical and experimental surface static pressure and centerline velocity distributions have also been made for the curved-plate geometry with $H=4$, but the agreement is not as good as that shown in Fig. 12. This discrepancy is attributed to the inaccurate variation with H of the length scales postulated in Ref. 6. Currently, with the availability of hot-wire anemometer test data, which were not available when the l_D and l_μ distributions were specified, more precise length scale variations can be formulated to provide a reliable prediction of the planar impinging jet flowfield in ground effect for arbitrary values of H and Re.

Summary

An experimental and theoretical study has been undertaken to determine the flow characteristics associated with a planar turbulent incompressible impinging jet in ground effect. The principal emphasis has been to gain an understanding of entrainment-induced suck-down forces on a simulated fuselage undersurface.

Both the measured and computed surface static pressure distributions reflect a strong influence on the jet height above ground and on the shape of the undersurface (either flat or contoured). The experimental data also show that for close ground effect, $H\leq 2$, there is a significant acceleration in the impingement flow on either side of the stagnation point, giving rise to below-ambient pressures on the ground plane.

The computed primary and primitive variables show the expected qualitative features of the flowfield. Specifically, these include the entrained flow into the free-jet region, characteristic boundary-layer development on the upper and lower surfaces, including separation on the former, and a sharp change in pressure within the impingement region. Quantitative agreement of the calculated and measured surface pressures and jet centerline velocity is good for $H=2$, but diverges as the jet height above ground is increased to 4.

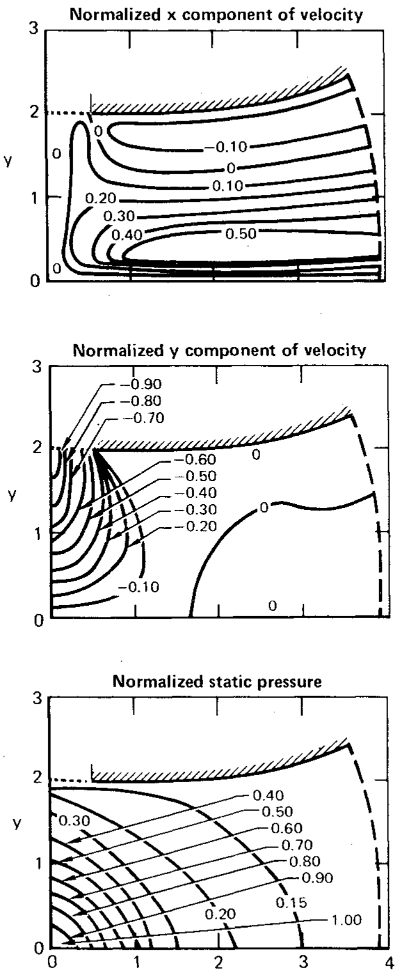

Fig. 11 Primitive flow variables for the curved-plate geometry ($H=2$, $W=3.68$, $Re=100{,}000$).

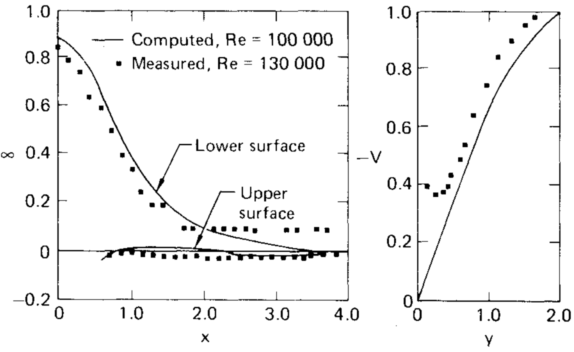

a) Surface static pressure variations

b) Centerline velocity variation

Fig. 12 Comparisons of computed and measured flow properties for the planar impinging jet, $H=2$.

This divergence is attributed to postulated length scale distributions in the one-equation turbulence model, which do not provide a correct variation of the turbulence field with H. Current work is directed toward improving these length scale distributions on the basis of recently acquired hot-wire anemometer data. If these modifications do not prove to be satisfactory, a more complete two-equation model of turbulence which does not require specification of the length scales will be introduced into the calculation procedure.

With the completion of a predicted scheme for the incompressible impinging jet, the analysis will be extended to the case of compressible flow. Such an extension is warranted, since, in reality, the fluid in the lift jet is at a temperature much higher than that of the surrounding fluid, and the immediate flowfield has large density gradients. For a jet in ground effect, the resulting effects can be significant, since density variations between the ambient air and the less dense lift jet have an influence on the entrainment. Also, buoyant forces act on the wall-jets and tend to induce wall-jet vertical liftoff (separation). A complementary test program will be conducted to investigate the accuracy of these calculations.

The final impinging jet configuration to be considered in the current MDRL VTOL aircraft flowfield investigation is an axisymmetric jet issuing from a flat surface which is then vectored, providing a 3-D flow problem. Entrainment and wall-jet characteristics obtained from such an analysis should provide more detailed insight into the propulsion-induced flows around VTOL aircraft.

Acknowledgment

The authors acknowledge the contribution of F. W. Roos, McDonnell Douglas Research Labs., in the acquisition and reduction of the hot-wire anemometer test data. The experimental work was conducted under the McDonnell Douglas Independent Research and Development Program, and the analytical work under the Office of Naval Research Contract N00014-C-76-0494.

References

[1] Tani, I. and Komatsu, Y., "Impingement of a Round Jet on a Flat Surface," *Proceedings of the Eleventh International Congress of Applied Mechanics*, 1966, pp. 672-676.

[2] du P. Donaldson, C. and Snedeker, R. S., "A Study of Free Jet Impingement. Part 1. Mean Properties of Free and Impinging Jets," *Journal of Fluid Mechanics*, Vol. 45, Part 2, January 30, 1971, pp. 281-319.

[3] Gray, L. and Kisielowski, E., "Practical Engineering Methods for Predicting Hot Gas Reingestion Characteristics of V/STOL Aircraft Jet-Lift Engines," NASA CR 111845, Feb. 1971.

[4] Bradbury, L.J.S., "The Impact of an Axisymmetric Jet onto a Normal Ground," *Aeronautical Quarterly*, Vol. 23, May 1972, pp. 141-147.

[5] Wolfshtein, M., "Convection Processes in Turbulent Impinging Jets," Report SF/R/2, Dept. of Mechanical Engineering, Imperial College of Science and Technology, Nov. 1967.

[6] Bower, W. W. and Kotansky, D. R., "A Navier-Stokes Analysis of the Two-Dimensional Ground Effects Problem," AIAA Paper 76-621, AIAA/SAE 12th Propulsion Conference, Palo Alto, Calif., 26-28 July, 1976.